Full control of qubit rotations in a voltage-biased superconducting flux qubit

Luca Chirolli and Guido Burkard
Department of Physics and Astronomy, University of Basel, Klingelbergstrasse 82, CH-4056 Basel, Switzerland
(Received 22 June 2006; revised manuscript received 4 September 2006; published 15 November 2006)

We study a voltage-controlled version of the superconducting flux qubit [Chiorescu *et al.*, Science **299**, 1869 (2003)] and show that full control of qubit rotations on the entire Bloch sphere can be achieved. Circuit graph theory is used to study a setup where voltage sources are attached to the two superconducting islands formed between the three Josephson junctions in the flux qubit. Applying a voltage allows qubit rotations about the y axis, in addition to pure x and z rotations obtained in the absence of applied voltages. The orientation and magnitude of the rotation axis on the Bloch sphere can be tuned by the gate voltages, the external magnetic flux, and the ratio α between the Josephson energies of the junctions via a flux-tunable junction. We compare the single-qubit control in the known regime $\alpha<1$ with the unexplored range $\alpha>1$ and estimate the decoherence due to voltage fluctuations.

DOI: 10.1103/PhysRevB.74.174510 PACS number(s): 74.50.+r, 03.67.Lx, 85.25.Cp

I. INTRODUCTION

Superconducting (SC) circuits can exhibit a great variety of quantum mechanical phenomena and are studied for their potential as devices for quantum information processing. Several different circuit implementations of a SC quantum bit (qubit) have been investigated both theoretically and experimentally.[1,2]

A prototype of a SC flux qubit, characterized by a working regime in which the Josephson energy dominates over the charging energy, $E_J \gg E_C$, has been theoretically designed and experimentally realized,[3–9] showing quantum superposition and coherent evolution of two macroscopic states carrying opposite persistent currents that represent the qubit states. The flux qubit state is related to a magnetic moment, and is thus typically controlled via the application of external magnetic fields which create magnetic flux through the loop(s) in the circuit. An advantage of flux qubits is their relative insensitivity to charge fluctuations that can lead to fast decoherence,[10–12] while magnetic fluctuations are typically more benign.

A second type of SC qubits, the so called charge qubits,[13–17] operates in the limit in which the charge energy dominates, $E_C \gg E_J$, thus being relatively insensitive to magnetic fluctuations, while having a well defined value of the charge on a SC island, in which the presence or absence of an extra Cooper pair determines the state of the qubit. The intermediate regime in which the Josephson and charge energies are comparable, $E_J \approx E_C$, has been investigated and realized in the "quantronium."[18] Another type of qubit is the Josephson, or phase, qubit, consisting of a single junction.[19]

In this paper, we investigate the possibility of enhancing the control of a SC flux qubit via the application of electrostatic gates.[3,20,21] We study the flux qubit proposed by Orlando *et al.*[3] While in Ref. 3, the effect of any applied voltages was kept low in order to avoid charge noise, we explore the possibility of making use of the offset gate charge as an additional control variable. We define two device parameters. Assuming for simplicity two Josephson junctions to have equal Josephson energies ($E_{J1}=E_{J2}=E_J$), the first parameter is given by the ratio $\alpha=E_{J3}/E_J$ between the Josephson energy of the third junction and the remaining two junctions. The regime of interest here is $0.5<\alpha\lesssim 1.5$ although in principle larger values are possible. The second parameter is the ratio between the Josephson energy and the charging energy, E_J/E_C which for flux qubits is typically about 10 or larger. We analyze the role of these parameters in detail and, in addition to the well-studied regime $\alpha<1$, also explore the opposite regime $\alpha>1$. Particular effort is spent looking for a single-qubit Hamiltonian in which an effective pseudomagnetic field couples to all three components of the pseudospin represented by the circuit. A charge qubit in which a σ_y term appears in the single-qubit Hamiltonian has been proposed in Ref. 22. The possibility of changing the relative phase of the qubit states, together with the capability to flip them, allows full control over the qubit. Full control on the Bloch sphere is thought to be very useful in the field of adiabatic quantum computation.[23–25]

Circuit theory provides us with a systematic and universal method for analyzing any electrical circuit that can be represented by lumped elements.[26–29] Through the language of a graph theoretic formalism, Kirchhoff's laws and the Hamiltonian of the circuit are written in terms of a set of independent canonical coordinates that can easily be quantized. The formalism of Refs. 26–28 is particularly suited for studying circuits containing superconducting elements, like Josephson junctions, that are treated as nonlinear inductors. Here, we make use of the extended circuit theory that accounts for charging effects and can be applied both for charge and flux qubits.[27]

Our main result is the identification of the parameter range for α and E_J/E_C in the voltage-controlled flux qubit in which the single qubit Hamiltonian acquires a σ_y term in addition to the σ_x and σ_z terms, thus allowing full control of the qubit rotations on the Bloch sphere. In this regime, we compute the dependence of the single-qubit Hamiltonian on the applied voltages V_1 and V_2. For the quantitative analysis of the qubit dynamics we calculate the tunneling amplitudes appearing in the Hamiltonian as functions of the device parameters.

The paper is structured as follows. In Sec. II we briefly review circuit theory[26–29] and apply it to the circuit of Fig. 2 to find its Hamiltonian. Section III contains the derivation of

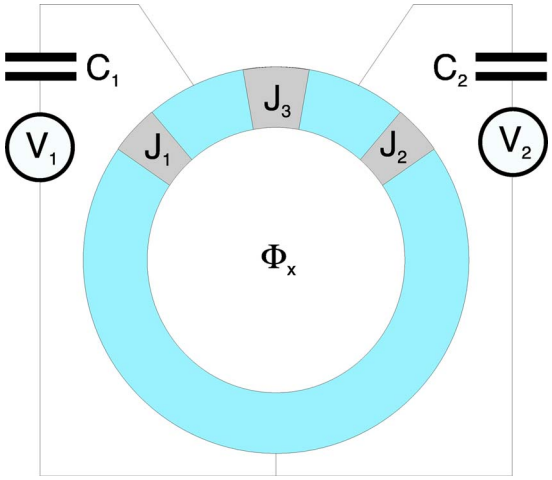

FIG. 1. (Color online) The voltage-biased SC flux qubit (schematic). The circuit consists of a SC ring with three Josephson junctions J_1, J_2, and J_3, threaded by an external magnetic flux Φ_x. The Josephson energy of the middle junction J_3 differs from the other two by a factor of α. A voltage bias V_i is applied to each of the two islands formed by the three junctions via a capacitor C_i.

the effective periodic potential in the Born-Oppenheimer approximation. In Sec. IV, we address the quantum dynamics of the circuit and find localized solutions in the periodic potential. In Sec. V we apply Bloch's theory in a tight-binding approximation to find general solutions in the presence of a voltage bias. Section VI describes the calculation of the tunneling matrix elements appearing in the qubit Hamiltonian and their dependence on the device parameters α and E_J/E_C. In Sec. VII, we explore the regime $\alpha > 1$ and show that a full control on the qubit Hamiltonian is feasible. In Sec. VIII, we study the decoherence of the qubit due to the attached voltage sources. Finally, Sec. IX contains a summary of our results and conclusions.

II. THE CIRCUIT

Here we study a version of the Delft flux qubit[3,7] with an additional voltage control (Fig. 1). Typically, such a qubit circuit also comprises a readout superconducting quantum interference device (SQUID) which can surround or be attached to the qubit. We concentrate on the qubit itself here and do not include the SQUID in our analysis because the presence of a readout circuit does not alter the analysis and results for single-qubit control presented here. A circuit representation of the studied device is shown in Fig. 2. The main loop contains three Josephson junctions and the loop self-inductance (K), and is threaded by an external magnetic flux Φ_x. The junctions form two SC islands to which electrostatic gates with capacitance C_1 and C_2 are attached and voltages V_1 and V_2 are applied. The voltage sources are the elements in the circuit that are not present in a regular flux qubit. As long as the junctions are built in such a way that the Josephson energy dominates, $E_J \gg E_C$, the qubit is encoded in the orientation of the circulating persistent current, as in Refs. 3 and 7.

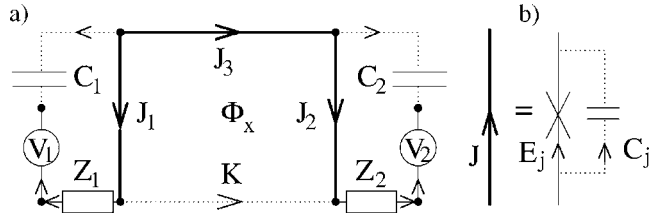

FIG. 2. (a) Circuit of a voltage-biased flux qubit (Fig. 1). The main loop contains three Josephson junctions and a (chord) inductance (K). An external magnetic flux Φ_x threads the SC loop. The junctions J_1 and J_2 are biased by two electrostatic gates, representing the main feature of the circuit. Solid lines represent the tree of the circuit graph, while dotted lines are the chords. (b) Each thick solid line represents a Josephson junction shunted by a capacitance C_J.

We represent the circuit as the oriented graph $\mathcal{G}$ shown in Fig. 2(a), consisting of $N=8$ nodes (black dots) n_i $(i=1,\ldots,8)$ and $B=13$ branches (thin lines) b_i $(i=1,\ldots,13)$, in which each branch b_i represents one of the following lumped circuit elements: a (bare) Josephson junction J, capacitance C, inductance K, voltage source V, and impedance Z. The impedances Z_1 and Z_2 model the imperfect voltage sources attached from outside to the quantum circuit. Every Josephson junction (thick line) consists of two branches: a bare Josephson junction (J) and the junction capacitance (C_J) as indicated in Fig. 2(b). In addition to these two elements, a Josephson junction can also be combined with a shunt resistance.[26] However, these resistances are typically very large and can often be neglected; they are not of interest here. The circuit graph $\mathcal{G}$ is divided in two parts. The *tree* is a loop-free subgraph which connects all nodes of the circuit and it is represented by solid lines in Fig. 2. All the branches f_i $(i=1,\ldots,F)$ that do not belong to the tree are called *chords* and are represented by dotted lines in Fig. 2. In the present case, the number of chords, not counting the junction capacitances C_J, is $F=3$. There can in principle be inductances contained both in the tree and in the chords which considerably complicate the analysis.[26] However, in our case there are no inductances in the tree (no L inductances), so that our analysis is much simpler than the general one. From now on, we make use of the fact that the circuit graph Fig. 2 has no inductances in its tree. When a chord is added to the tree, it gives rise to a unique loop, a *fundamental loop*. In other words, the set of fundamental loops $\mathcal{F}_i$ of the graph consists of all loops which contain exactly one chord f_i. The topological information about the graph is encoded in the fundamental loop matrix $\mathbf{F}^{(L)}$ of the circuit $(i=1,\ldots,F;\ j=1,\ldots,B)$,

$$\mathbf{F}_{ij}^{(L)} = \begin{cases} 1, & \text{if } b_j \in \mathcal{F}_i \ \text{(same direction)}, \\ -1, & \text{if } b_j \in \mathcal{F}_i \ \text{(opposite direction)}, \\ 0, & \text{if } b_j \notin \mathcal{F}_i, \end{cases} \tag{1}$$

where the direction of the fundamental loop $\mathcal{F}_i$ is given by the direction of its defining chord f_i. The currents $\mathbf{I}=(I_1,\ldots,I_B)$ and the voltages $\mathbf{V}=(V_1,\ldots,V_B)$ associated

with the branches of the graph are divided into tree and chord currents and voltages,

$$\mathbf{I} = (\mathbf{I}_{\mathrm{tr}}, \mathbf{I}_{\mathrm{ch}}), \quad \mathbf{V} = (\mathbf{V}_{\mathrm{tr}}, \mathbf{V}_{\mathrm{ch}}). \tag{2}$$

With the division into tree and chord branches, the fundamental loop matrix assumes the block form

$$\mathbf{F}^{(L)} = (-\mathbf{F}^{T}|\mathbb{1}). \tag{3}$$

We further split up the current and voltage vectors according to the type of branch (Ref. 27),

$$\mathbf{I}_{\mathrm{tr}} = (\mathbf{I}_J, \mathbf{I}_V, \mathbf{I}_Z), \quad \mathbf{I}_{\mathrm{ch}} = (\mathbf{I}_{C_J}, \mathbf{I}_C, \mathbf{I}_K),$$

$$\mathbf{V}_{\mathrm{tr}} = (\mathbf{V}_J, \mathbf{V}_V, \mathbf{V}_Z), \quad \mathbf{V}_{\mathrm{ch}} = (\mathbf{V}_{C_J}, \mathbf{V}_C, \mathbf{V}_K), \tag{4}$$

such that the matrix $\mathbf{F}$ acquires the subblock form

$$\mathbf{F} = \begin{pmatrix} \mathbb{1} & \mathbf{F}_{JC} & \mathbf{F}_{JK} \\ 0 & \mathbf{F}_{VC} & \mathbf{F}_{VK} \\ 0 & \mathbf{F}_{ZC} & \mathbf{F}_{ZK} \end{pmatrix}. \tag{5}$$

By inspection of Fig. 2, one finds the loop submatrices of the circuit according to the rule in Eq. (1),

$$\mathbf{F}_{JC} = \begin{pmatrix} 1 & 0 \\ 0 & 1 \\ 0 & 0 \end{pmatrix}, \quad \mathbf{F}_{JK} = \begin{pmatrix} -1 \\ 1 \\ 1 \end{pmatrix},$$

$$\mathbf{F}_{VC} = \mathbf{F}_{ZC} = \begin{pmatrix} 1 & 0 \\ 0 & 1 \end{pmatrix}, \quad \mathbf{F}_{VK} = \mathbf{F}_{ZK} = \begin{pmatrix} 0 \\ 0 \end{pmatrix}. \tag{6}$$

With Eq. (3), Kirchhoff's laws have the compact form

$$\mathbf{F}\mathbf{I}_{\mathrm{ch}} = -\mathbf{I}_{\mathrm{tr}}, \tag{7}$$

$$\mathbf{F}^{T}\mathbf{V}_{\mathrm{tr}} = \mathbf{V}_{\mathrm{ch}} - \dot{\mathbf{\Phi}}_x, \tag{8}$$

where $\mathbf{\Phi}_x = (\Phi_1, \ldots, \Phi_F)$ is the vector of externally applied fluxes. Only loops with a nonzero inductance are susceptible to an external magnetic flux, thus only one external flux needs to be considered here, $\mathbf{\Phi}_x = (0, 0, \Phi_x)$.

The SC phase differences across the junctions $\boldsymbol{\varphi} = (\varphi_1, \varphi_2, \varphi_3)$ are related to the canonical variables, the fluxes $\mathbf{\Phi}$, through the relation

$$\boldsymbol{\varphi} = 2\pi \frac{\mathbf{\Phi}}{\Phi_0}, \tag{9}$$

while the canonically conjugate momenta are the charges $\mathbf{Q} = (Q_1, Q_2)$ on the junction capacitance. Using circuit theory[27] and ignoring the dissipative circuit elements Z_1 and Z_2 for the moment, we find the following Hamiltonian of the circuit Fig. 2:

$$\mathcal{H}_S = \frac{1}{2}(\mathbf{Q} - \mathbf{C}_V\mathbf{V}_V)^T\mathcal{C}^{-1}(\mathbf{Q} - \mathbf{C}_V\mathbf{V}_V) + \mathcal{U}(\mathbf{\Phi}), \tag{10}$$

$$\mathcal{U}(\mathbf{\Phi}) = -\mathbf{E}_J \cos 2\pi \frac{\mathbf{\Phi}}{\Phi_0} + \frac{1}{2}\mathbf{\Phi}^{\mathrm{T}}\mathbf{M}_0\mathbf{\Phi} + \mathbf{\Phi}^{\mathrm{T}}\mathbf{N}\mathbf{\Phi}_x, \tag{11}$$

where we have defined $\cos \boldsymbol{\varphi} = (\cos\varphi_1, \cos\varphi_2, \cos\varphi_3)$. The Josephson energy matrix is given as follows:

$$\mathbf{E}_J = \left(\frac{\Phi_0}{2\pi}\right)^2 \mathbf{L}_J^{-1} = \mathrm{diag}(E_J, E_J, \alpha E_J), \tag{12}$$

where $\Phi_0 = h/2e$ is the SC quantum of magnetic flux. We assume that the Josephson energies and capacitances of the junctions J_1 and J_2 are equal, $E_{J1} = E_{J2} \equiv E_J$ and $C_{J1} = C_{J2} \equiv C_J$, and we define the ratio $\alpha = E_{J3}/E_J$. The capacitance matrices of the circuit are

$$\mathbf{C}_J = \mathrm{diag}(C_J, C_J, C_{J3}), \quad \mathbf{C} = \mathrm{diag}(C_1, C_2). \tag{13}$$

The source voltage vector is defined as $\mathbf{V}_V = (V_1, V_2)$. The derived capacitance matrices $\mathcal{C}$ and $\mathbf{C}_V$ and the derived (inverse) inductance matrices $\mathbf{M}_0$ and $\mathbf{N}$ of Eq. (10) are given in the Appendix A.

III. BORN-OPPENHEIMER APPROXIMATION

We consider now the limit in which the chord inductance K is small compared to the Josephson inductances, $K \ll L_J$. By means of the Born-Oppenheimer approximation, we derive an effective two-dimensional potential as a function of two "slow" degrees of freedom. Our analysis follows closely that of Ref. 29. For $K \ll L_J$, the potential Eq. (11) gives rise to a hard constraint for the variables $\boldsymbol{\varphi}$, in the form of the linear equation

$$\mathbf{M}_0\boldsymbol{\varphi} + \mathbf{N}\varphi_x = 0, \tag{14}$$

where the external magnetic flux is written as $\varphi_x = 2\pi\Phi_x/\Phi_0$. The general solution of the Eq. (14),

$$\boldsymbol{\varphi} = \begin{pmatrix} \varphi_1 \\ \varphi_2 \\ \varphi_1 - \varphi_2 + \varphi_x \end{pmatrix}, \tag{15}$$

depends on the two variables φ_1 and φ_2 only. Thus, in the limit of small K, the dynamics are restricted to a plane in three-dimensional $\boldsymbol{\varphi}$ space. The potential, restricted to the plane, is then a function of φ_1 and φ_2 only (Ref. 3),

$$\mathcal{U}(\boldsymbol{\varphi}) = E_J[-\cos(\varphi_1) - \cos(\varphi_2) - \alpha\cos(\varphi_1 - \varphi_2 + \varphi_x)]. \tag{16}$$

A density plot of $\mathcal{U}$ for $\alpha = 0.8$ as a function of φ_1 and φ_2 is shown in the inset of Fig. 3. The minima of the potential are found by solving the equation $\mathrm{grad}\,\mathcal{U} = 0$, which yields (Ref. 3)

$$\sin\varphi_1 = -\sin\varphi_2 = -\sin\varphi^*, \tag{17}$$

where φ^* is the solution of the self-consistent equation

$$\sin\varphi^* = \alpha\sin(2\varphi^* + \varphi_x). \tag{18}$$

The potential forms two wells whose relative depth is determined by the value of the externally applied flux φ_x. In order

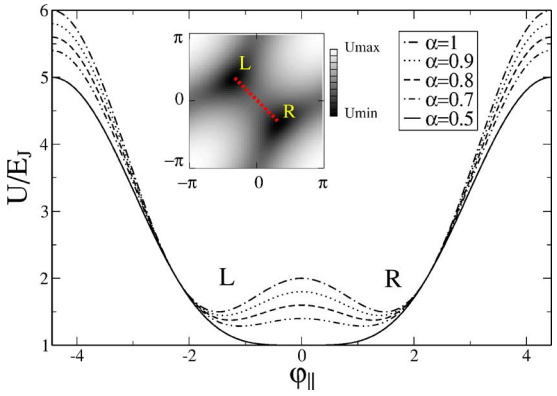

FIG. 3. (Color online) Plot of the potential $\mathcal{U}(\boldsymbol{\varphi})$ for $\varphi_x=\pi$ along the line $\varphi_1+\varphi_2=0$ as a function of $\varphi_\parallel=\frac{1}{\sqrt{2}}(\varphi_1-\varphi_2)$ for several values of α. In the curve for $\alpha=0.5$ the two minima are degenerate, while for $\alpha>0.5$ they split showing the double well. The inset is a density plot of the potential for $\alpha=0.8$, showing the two minima and the line $\varphi_1+\varphi_2=0$.

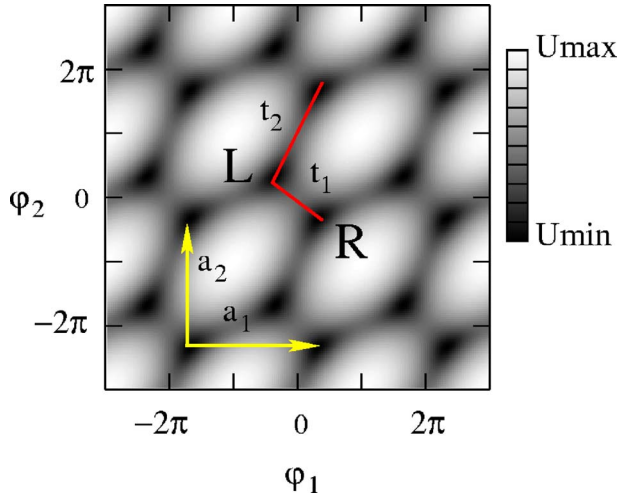

FIG. 4. (Color online) Density plot of the double well potential $U(\varphi_1,\varphi_2)$ in units of E_J for $\alpha=0.8$ on a logarithmic scale. The periodicity of the potential is evident; each unit cell contains two minima (black). The primitive vectors of the Bravais lattice are denoted $\mathbf{a}_1$ and $\mathbf{a}_2$ while t_1 and t_2 are the tunneling matrix elements between the nearest-neighbor minima.

to have a symmetric double well we choose $\varphi_x=\pi$ which yields two minima at the points $\boldsymbol{\varphi}_R=(\varphi^*,-\varphi^*)$ and $\varphi_L=(-\varphi^*,\varphi^*)$ with $\varphi^*=\arccos(1/2\alpha)>0$. If $\alpha>0.5$, then there are two distinct minima. Taking into account the periodicity of the potential, a complete set of solutions of Eq. (18) is $\boldsymbol{\varphi}=\pm(\varphi^*,-\varphi^*)^T+2\pi(n,m)$, with integer n, m. We plot the double well potential between the two minima in Fig. 3 for different values of α in the symmetric case $\varphi_x=\pi$.

IV. QUANTUM DYNAMICS

In this section, we look for localized solutions of the Schrödinger equation $\mathcal{H}\Psi=E\Psi$, with the Hamiltonian of Eq. (10). We expand the potential around the two minimum configurations, keeping contributions up to the second order in $\boldsymbol{\varphi}$, and solve the Schrödinger equation in these two different points (denoting them L and R for left and right). We obtain the quadratic Hamiltonian

$$\mathcal{H}_{L,R}=\tfrac{1}{2}[\mathbf{Q}^T\mathcal{C}^{-1}\mathbf{Q}+\boldsymbol{\Phi}^T\mathbf{L}^{-1}_{\mathrm{lin;L,R}}\boldsymbol{\Phi}], \tag{19}$$

where the linearized inductance $\mathbf{L}_{\mathrm{lin;L,R}}$ is defined

$$\mathbf{L}^{-1}_{\mathrm{lin;L,R}}=\mathbf{M}_0+\mathbf{L}_J^{-1}\cos\boldsymbol{\varphi}_{L,R}. \tag{20}$$

To simplify the kinetic part in Eq. (19), we perform a canonical transformation on the variable $\boldsymbol{\Phi}$ and its conjugate momentum $\mathbf{Q}$ (Ref. 29),

$$\boldsymbol{\Phi}=\sqrt{c}(\sqrt{\mathcal{C}}^{-1})^T\tilde{\boldsymbol{\Phi}},$$

$$\mathbf{Q}=\sqrt{\mathcal{C}}\tilde{\mathbf{Q}}/\sqrt{c}, \tag{21}$$

where c is an arbitrary unit capacitance (e.g., $c=C_J$). We define the diagonal matrix $\boldsymbol{\Omega}^2_{L,R}$ such that it satisfies

$$(\sqrt{\mathcal{C}}^{-1})^T\mathbf{L}^{-1}_{\mathrm{lin;L,R}}\sqrt{\mathcal{C}}^{-1}=\mathbf{O}^T\boldsymbol{\Omega}^2_{L,R}\mathbf{O}, \tag{22}$$

where $\mathbf{O}$ is an orthogonal matrix that diagonalizes the left-hand side (lhs) of Eq. (22). This allows us to further simplify the Hamiltonian by making the following canonical transformation, preserving the Poisson brackets:

$$\boldsymbol{\Phi}'=\mathbf{O}\tilde{\boldsymbol{\Phi}},\quad \mathbf{Q}'=\mathbf{O}\tilde{\mathbf{Q}}, \tag{23}$$

that leads us to the Hamiltonian,

$$\mathcal{H}_{L,R}=\tfrac{1}{2}(c^{-1}\mathbf{Q}'^2+\boldsymbol{\Phi}'^T\boldsymbol{\Omega}^2_{L,R}\boldsymbol{\Phi}'). \tag{24}$$

In the case of a symmetric potential (when $\varphi_x=\pi$), the matrices $\mathbf{L}_{\mathrm{lin;L,R}}$ of the linearized problem are equal,

$$\mathbf{L}_{\mathrm{lin;L}}=\mathbf{L}_{\mathrm{lin;R}},\quad \text{and } \boldsymbol{\Omega}_L=\boldsymbol{\Omega}_R, \tag{25}$$

hence we drop the subscript L and R for simplicity.

We quantize the Hamiltonian by imposing the canonical commutation relations,

$$[\Phi_i,Q_j]=i\hbar\,\delta_{ij}, \tag{26}$$

where Φ_i and Q_j are the components of the vectors $\boldsymbol{\Phi}$ and $\mathbf{Q}$, respectively. The ground-state wave function is the Gaussian,

$$\Psi_\alpha(\boldsymbol{\varphi})=\left(\frac{\det\mathcal{M}}{\pi^2}\right)^{1/4}\exp\left[-\frac{1}{2}(\boldsymbol{\varphi}-\boldsymbol{\varphi}_\alpha)^T\mathcal{M}(\boldsymbol{\varphi}-\boldsymbol{\varphi}_\alpha)\right], \tag{27}$$

where α=L, R, and

$$\mathcal{M}=\frac{1}{\hbar}\left(\frac{\Phi_0}{2\pi}\right)^2\sqrt{\mathcal{C}}\mathbf{O}^T\boldsymbol{\Omega}\mathbf{O}\sqrt{\mathcal{C}}. \tag{28}$$

For the wave function overlap integral between the left and right state, $S=\langle\Psi_L|\Psi_R\rangle$, we find

$$S=\exp\{-\tfrac{1}{4}\Delta\boldsymbol{\varphi}^T\mathcal{M}\Delta\boldsymbol{\varphi}\}, \tag{29}$$

where $\Delta\boldsymbol{\varphi}=\boldsymbol{\varphi}_R-\boldsymbol{\varphi}_L=2\arccos(1/2\alpha)(1,-1)$ is the distance between the right (R) and left (L) potential minima (Fig. 4).

V. BLOCH THEORY

Given the periodicity of the problem Eq. (10) with the potential Eq. (16) in the Born-Oppenheimer approximation, an important question concerns the boundary conditions of the problem, i.e., the choice of the appropriate Hilbert space. The question is whether the domain of $\boldsymbol{\varphi}$ should be the infinite plane or the square $T=[-\pi,\pi)^2$ with periodic boundary conditions. This question has been discussed extensively in the literature.[30–32] Since in our case, a shift of φ_1 or φ_2 by 2π creates a state which is physically indistinguishable from the one before the shift, we choose the compact domain T and impose periodic boundary conditions on the wave function. However, we are going to extend the domain to the infinite domain in order to facilitate the calculation.

A. The periodic problem

The approximate solutions constructed in Sec. IV are a good starting point, but they are insensitive to the boundary conditions. However, the boundary conditions are essential if finite bias voltages $\mathbf{V}_V$ are to be taken into account. The problem at hand is defined on the square with side 2π (see inset of Fig. 3) with periodic boundary conditions; i.e., the phases $\boldsymbol{\varphi}=(\varphi_1,\varphi_2)^T$ are in the compact domain $T=[-\pi,\pi)^2$ and the wave function at opposite edges needs to be identical, $\Psi(-\pi,\varphi_2)=\Psi(\pi,\varphi_2)$ and $\Psi(\varphi_1,-\pi)=\Psi(\varphi_1,\pi)$, such that T acquires the topology of a torus. If the boundary conditions are ignored, e.g., in the case where the wave function is known to be vanishingly small at the boundary, then the bias voltages $\mathbf{V}_V$ in the Hamiltonian Eq. (10) can be removed completely with a gauge transformation and the solutions will be independent of $\mathbf{V}_V$.

We proceed as follows: We first solve the problem Eq. (10) in the infinite two-dimensional plane and then choose those solutions that satisfy the periodic boundary conditions and then restrict them to the compact domain T. We choose this approach because the problem on the infinite domain is well known: the solutions $\psi_{\alpha\mathbf{k}}$ are given by Bloch's theorem for the motion of a particle in a crystal and satisfy

$$\psi_{\alpha\mathbf{k}}(\boldsymbol{\varphi}+2\pi\mathbf{m})=e^{2\pi i\mathbf{m}\cdot\mathbf{k}}\psi_{\alpha\mathbf{k}}(\boldsymbol{\varphi}), \tag{30}$$

for $\mathbf{m}=(m_1,m_2)$ with integer m_1 and m_2. The minima of our potential, Eq. (16), define a two-dimensional square Bravais lattice with a two-point basis, which looks like a sheared hexagonal lattice (although it is a square lattice). The lattice and its primitive vectors $\mathbf{a}_1=(2\pi,0)$ and $\mathbf{a}_2=(0,2\pi)$ are shown in Fig. 4. The lattice basis is given by the vectors $\mathbf{b}_\mathrm{L}=(0,0)$ and $\mathbf{b}_\mathrm{R}=2(\varphi^*,-\varphi^*)$. Each lattice point can be identified by the Bravais lattice vector $\mathbf{n}$ and the basis index $\alpha=$L, R. As indicated above, not all the Bloch functions satisfying the Schrödinger equation on the infinite domain have a physical meaning, but only those that are also 2π periodic. In the case of zero applied voltage bias, the only value of $\mathbf{k}$ yielding to a periodic wave function is $\mathbf{k}=\mathbf{0}$.

B. Tight-binding approximation

In order to construct approximate Bloch states, we first form localized Wannier orbitals ϕ_α by orthonormalizing the localized solutions Ψ_α ($\alpha=$L,R) from Eq. (27). These Wannier orbitals are centered at arbitrary lattice points, $\phi_{\alpha\mathbf{n}}(\boldsymbol{\varphi})=\phi_\alpha(\boldsymbol{\varphi}-2\pi\mathbf{n})$ and satisfy the orthonormality relations

$$\langle\phi_{\alpha\mathbf{n}}|\phi_{\beta\mathbf{m}}\rangle=\delta_{\alpha\beta}\delta_{\mathbf{nm}}. \tag{31}$$

The Bloch states are then related to the Wannier orbitals via a Fourier transform,

$$\psi_{\alpha\mathbf{k}}(\boldsymbol{\varphi})=\sum_{\mathbf{n}\in\mathbb{Z}^2}e^{2\pi i\mathbf{k}\cdot\mathbf{n}}\phi_{\alpha\mathbf{n}}(\boldsymbol{\varphi}), \tag{32}$$

$$\phi_{\alpha\mathbf{n}}(\boldsymbol{\varphi})=\int_{\mathrm{FBZ}}d\mathbf{k}e^{-2\pi i\mathbf{k}\cdot\mathbf{n}}\psi_{\alpha\mathbf{k}}(\boldsymbol{\varphi}), \tag{33}$$

where the integration in Eq. (33) is over the first Brillouin zone (FBZ), i.e., $k_i\in[-1/2,1/2)$. The label α plays the role of the energy band label in Bloch theory. The Bloch states $\psi_{\alpha\mathbf{k}}$ form a complete set of orthonormal states in $\mathbf{k}$ space, where $k_i\in[-1/2,1/2)$,

$$\langle\psi_{\alpha\mathbf{k}}|\psi_{\beta\mathbf{q}}\rangle=\delta_{\alpha\beta}\delta(\mathbf{k}-\mathbf{q}), \tag{34}$$

$$\sum_\alpha\int d\mathbf{k}|\psi_{\alpha\mathbf{k}}\rangle\langle\psi_{\alpha\mathbf{k}}|=\mathbb{1}. \tag{35}$$

For the completeness relation Eq. (35) to hold, we must sum over all bands α, corresponding to a complete set of Wannier functions. Here, in order to describe the low-energy physics of the system, we restrict ourselves to the two lowest bands $\alpha=$L, R, related to the left and right potential minimum in the unit cell, and neglect higher excited states of the double wells. This restriction is justified if the energy gap between the lowest two states is much smaller than the gap between the two lowest and all higher states (see Table I). We normalize the Bloch functions on the unit cell T,

$$\int_T d\boldsymbol{\varphi}|\psi_{\mathbf{k}\alpha}(\boldsymbol{\varphi})|^2=1. \tag{36}$$

Now we can expand the Hamiltonian in the Bloch function basis with Eq. (35), and then apply Eq. (32),

$$\begin{aligned}\mathcal{H}&\simeq\sum_{\alpha\beta}\int d\mathbf{k}d\mathbf{q}|\psi_{\alpha\mathbf{k}}\rangle\langle\psi_{\alpha\mathbf{k}}|\mathcal{H}|\psi_{\beta\mathbf{q}}\rangle\langle\psi_{\beta\mathbf{q}}|\\&=\sum_{\alpha\beta}\int d\mathbf{k}d\mathbf{q}\mathcal{H}^{\alpha\beta}_{\mathbf{kq}}|\psi_{\alpha\mathbf{k}}\rangle\langle\psi_{\beta\mathbf{q}}|,\end{aligned} \tag{37}$$

where the approximation in the first line consists in omitting bands that are energetically higher than $\alpha=$L, R (see above). The matrix elements of the Hamiltonian in the Bloch basis are

$$\mathcal{H}^{\alpha\beta}_{\mathbf{kq}}=\sum_{\mathbf{n},\mathbf{m}\in\mathbb{Z}^2}e^{-2\pi i(\mathbf{k}\cdot\mathbf{n}-\mathbf{q}\cdot\mathbf{m})}\langle\phi_{\alpha\mathbf{n}}|\mathcal{H}|\phi_{\beta\mathbf{m}}\rangle. \tag{38}$$

For fixed $\mathbf{k}$ and $\mathbf{q}$, Eq. (38) is reduced to a 2×2 Hermitian matrix. The main contributions to Eq. (38) stem from either tunneling between the two sites in the same unit cell (intracell) or between site L in one cell and site R in an adjacent

TABLE I. Values of t_1, t_2, their ratio t_2/t_1, the energy gap $|\Delta|_0$ at zero applied voltage, and the minimum of the gap $|\Delta|_{\min}$ for a series of values of α and E_J/E_C. In the last column we report the ratio of the energy difference E_{12} between the second and first excited state and the qubit gap $|\Delta|_0$.

α	E_J/E_C	t_2/t_1	t_1/E_J $\times 10^{-3}$	t_2/E_J $\times 10^{-5}$	$\lvert\Delta\rvert_0/E_J$	$\lvert\Delta\rvert_{\min}/\lvert\Delta\rvert_0$	$E_{12}/\lvert\Delta\rvert_0$
0.80	35	0.0062	−2.9	−1.8	0.0059	0.98	82
0.85	30	0.030	−1.9	−5.8	0.0040	0.88	126
0.90	25	0.12	−1.5	−18	0.0037	0.61	149
0.95	20	0.39	−1.5	−59	0.0054	0.12	116
1.00	15	0.97	−2.05	−198	0.012	0	61
1.05	10	1.77	−4.2	−740	0.038	0	24

cell (intercell), see Fig. 4. For the off-diagonal element we can write

$$\mathcal{H}^{\mathrm{LR}}_{\mathbf{kq}} \simeq \sum_{\mathbf{n}\in\mathbb{Z}^2} e^{-2\pi i(\mathbf{k}-\mathbf{q})\cdot\mathbf{n}}[\langle\phi_{\mathrm{Ln}}|\mathcal{H}|\phi_{\mathrm{Rn}}\rangle + e^{-2\pi i q_1}\langle\phi_{\mathrm{Ln}}|\mathcal{H}|\phi_{\mathbf{Rn}-\mathbf{e}_1}\rangle + e^{2\pi i q_2}\langle\phi_{\mathrm{Ln}}|\mathcal{H}|\phi_{\mathbf{Rn}+\mathbf{e}_2}\rangle], \tag{39}$$

where $\mathbf{e}_1=(1,0)$ and $\mathbf{e}_2=(0,1)$. Due to the lattice periodicity, the quantities (see Fig. 4)

$$\epsilon_0 = \langle\phi_{L(R)\mathbf{n}}|\mathcal{H}|\phi_{L(R)\mathbf{n}}\rangle, \tag{40}$$

$$t_1 = \langle\phi_{L(R)\mathbf{n}}|\mathcal{H}|\phi_{R(L)\mathbf{n}}\rangle, \tag{41}$$

$$t_2 = \langle\phi_{L(R)\mathbf{n}}|\mathcal{H}|\phi_{R(L)\mathbf{n}-\mathbf{e}_1}\rangle \tag{42}$$

$$= \langle\phi_{L(R)\mathbf{n}}|\mathcal{H}|\phi_{R(L)\mathbf{n}+\mathbf{e}_2}\rangle, \tag{43}$$

are independent of the lattice site $\mathbf{n}$, and thus from Eq. (38), we find $\mathcal{H}^{\alpha\beta}_{\mathbf{kq}} \simeq \delta(\mathbf{k}-\mathbf{q})\mathcal{H}^{\alpha\beta}_{\mathbf{k}}$. We can now write the 2×2 Hamiltonian as follows:

$$\mathcal{H}_{\mathbf{k}} = \epsilon_0 \mathbb{1} + \frac{1}{2}\begin{pmatrix} 0 & \Delta(\mathbf{k})^* \\ \Delta(\mathbf{k}) & 0 \end{pmatrix}, \tag{44}$$

$$\Delta(\mathbf{k}) = 2[t_1 + t_2(e^{2\pi i k_1} + e^{-2\pi i k_2})]. \tag{45}$$

The equality in Eq. (43) is due to the invariance of the potential under the transformation $(\varphi_1,\varphi_2)\to -(\varphi_2,\varphi_1)$ and it is valid also in the $\varphi_x \neq \pi$ case. The eigenvalues of the problem are

$$\epsilon_{\pm}(\mathbf{k}) = \epsilon_0 \pm \tfrac{1}{2}|\Delta(\mathbf{k})|, \tag{46}$$

and represent a typical two-band dispersion relation. In the case of zero external applied voltage only the $\mathbf{k}=\mathbf{0}$ Bloch functions satisfy the correct boundary conditions, i.e., are periodic. For $\mathbf{k}=\mathbf{0}$ we recognize the qubit Hamiltonian that, in the symmetric double well case, is given by a σ_x term (Ref. 3),

$$\mathcal{H} = \epsilon_0 + (t_1 + 2t_2)\sigma_x. \tag{47}$$

C. Effect of a voltage bias

Now, we study the case with an (nonzero) external bias voltage. Given the Bloch function $\psi_{\alpha\mathbf{k}}$ that satisfies the Schrödinger equation for the Hamiltonian Eq. (10) for zero applied voltages, $\mathbf{V}_V=\mathbf{0}$, we find for the solution a wave function for finite voltages $\mathbf{V}_V\neq\mathbf{0}$,

$$u_{\alpha\mathbf{k}}(\boldsymbol{\varphi}) = e^{-i\boldsymbol{\varphi}\cdot\mathbf{Q}_g/2e}\psi_{\alpha\mathbf{k}}(\boldsymbol{\varphi}), \tag{48}$$

where we have defined the gate charge vector as $\mathbf{Q}_g=\mathbf{C}_V\mathbf{V}_V$. The above statement can be directly verified by substituting $u_{\alpha\mathbf{k}}$ from Eq. (48) into the Schrödinger equation with Eq. (10) while using $\psi_{\alpha\mathbf{k}}$ that solves the problem for $\mathbf{V}_V=\mathbf{0}$. The solutions in the presence of an applied voltage bias satisfy

$$u_{\alpha\mathbf{k}}(\boldsymbol{\varphi}+2\pi\mathbf{n}) = e^{2\pi i\mathbf{n}\cdot(\mathbf{k}-\mathbf{Q}_g/2e)}u_{\alpha\mathbf{k}}(\boldsymbol{\varphi}). \tag{49}$$

For the periodicity of the wave function on the compact domain, we have to choose $\mathbf{k}=\mathbf{Q}_g/2e$. This means that $u_{\alpha\mathbf{k}}$ is the periodic part of the Bloch function for $\mathbf{k}=\mathbf{Q}_g/2e$. By substituting this into Eqs. (44) and (45), we obtain the qubit Hamiltonian

$$\mathcal{H} = \frac{1}{2}[\mathrm{Re}(\Delta)\sigma_x + \mathrm{Im}(\Delta)\sigma_y + \epsilon\sigma_z] = \frac{1}{2}\mathbf{B}\cdot\boldsymbol{\sigma}, \tag{50}$$

where we have also included the effect of a (small) bias flux that tilts the double well, $\epsilon \simeq 2\sqrt{1-1/4\alpha^2}E_J(\varphi_x-\pi)$, where $\boldsymbol{\sigma}=(\sigma_x,\sigma_y,\sigma_z)$ are the Pauli matrices, and

$$\mathrm{Re}(\Delta) = 2[t_1 + 2t_2\cos(\pi k_+)\cos(\pi k_-)], \tag{51}$$

$$\mathrm{Im}(\Delta) = 4t_2\cos(\pi k_+)\sin(\pi k_-), \tag{52}$$

with $k_\pm=(C_1V_1\pm C_2V_2)/2e$. The eigenstates for $\epsilon=0$ are

$$|0\rangle = \frac{1}{\sqrt{2}}(-e^{-i\theta}|L\rangle + |R\rangle), \tag{53}$$

$$|1\rangle = \frac{1}{\sqrt{2}}(e^{-i\theta}|L\rangle + |R\rangle), \tag{54}$$

where $\tan\theta=\mathrm{Im}(\Delta)/\mathrm{Re}(\Delta)$. In Eq. (50), we have introduced the pseudofield $\mathbf{B}=(\mathrm{Re}(\Delta),\mathrm{Im}(\Delta),\epsilon)$.

VI. CALCULATION OF t_1 AND t_2

For a quantitative analysis of the single-qubit Hamiltonian Eq. (50), we have to calculate the tunneling matrix elements t_1 and t_2. In order to do so, we require a set of orthonormal Wannier functions on the infinite two-dimensional lattice defined by the potential $\mathcal{U}$, Eq. (11). We start from the nonorthogonal set of Gaussian orbitals $|\Psi_{\alpha\mathbf{n}}\rangle$ consisting of the solution Eq. (27), shifted by a lattice vector $\mathbf{n}$,

$$\Psi_{\alpha\mathbf{n}}(\boldsymbol{\varphi}) = \Psi_{\alpha}(\boldsymbol{\varphi} - 2\pi\mathbf{n}). \tag{55}$$

The orthonormalized Wannier functions can be written as a linear combination of these Gaussians,

$$|\phi_{\alpha\mathbf{n}}\rangle = \sum_{\mu=L,R,\mathbf{l}\in\mathbb{Z}^2} \mathcal{G}_{\mu\mathbf{l},\alpha\mathbf{n}}|\Psi_{\mu\mathbf{l}}\rangle. \tag{56}$$

To form a complete set of orthonormal functions the following relation must be satisfied:

$$\langle\phi_{\alpha\mathbf{n}}|\phi_{\beta\mathbf{m}}\rangle = (\mathcal{G}^{\dagger}S\mathcal{G})_{\alpha\mathbf{n},\beta\mathbf{m}} = \delta_{\alpha\beta}\delta_{\mathbf{nm}}, \tag{57}$$

where S is the (real and symmetric) overlap matrix,

$$S_{\alpha\mathbf{n},\beta\mathbf{m}} = \int d\boldsymbol{\varphi}\Psi_{\alpha\mathbf{n}}(\boldsymbol{\varphi})\Psi_{\beta\mathbf{m}}(\boldsymbol{\varphi}). \tag{58}$$

We solve Eq. (57) with

$$\mathcal{G}^T = \mathcal{G} = \sqrt{S^{-1}}. \tag{59}$$

The inverse of S exists due to its positive definiteness. The entries of the overlap matrix S are equal to 1 on the diagonal, whereas the off-diagonal elements are positive and $\ll 1$ because the orbitals $\Psi_{\alpha\mathbf{n}}$ are well localized. We define the matrix $S^{(1)}$ with all matrix elements $\ll 1$ via

$$S = \mathbb{1} + S^{(1)} = \mathbb{1} + \begin{pmatrix} S_{\mathrm{LL}} & S_{\mathrm{LR}} \\ S_{\mathrm{LR}}^T & S_{\mathrm{RR}} \end{pmatrix}, \tag{60}$$

and find, keeping only first order terms in $S^{(1)}$,

$$\mathcal{G} \simeq \sqrt{S^{-1}} \simeq \mathbb{1} - \frac{1}{2}S^{(1)}. \tag{61}$$

Note that S_{LL} and S_{RR} have zeros on the diagonal.

In our tight-binding approximation, we consider five unit cells, a center cell with its four nearest neighbors, corresponding to the lattice vectors $\{(0,0),(\pm1,0),(0,\pm1)\}$. This means that S and $\mathcal{G}$ are 10×10 matrices, which can also be expressed as 2×2 block matrices, each block of dimension 5×5. The two largest values are given by $s_1 = S_{\mathbf{Ln},\mathbf{Rn}}$ and $s_2 = S_{\mathbf{Ln},\mathbf{Rn}-\mathbf{e}_1} = S_{\mathbf{Ln},\mathbf{Rn}+\mathbf{e}_2}$ with the nearest neighbor cell. Taking only these two largest overlaps into account, we obtain $S_{\mathrm{LL}} = S_{\mathrm{RR}} \simeq 0$ and

$$S_{\mathrm{LR}} \simeq \begin{pmatrix} s_1 & s_2 & s_2 & 0 & 0 \\ 0 & s_1 & 0 & 0 & 0 \\ 0 & 0 & s_1 & 0 & 0 \\ s_2 & 0 & 0 & s_1 & 0 \\ s_2 & 0 & 0 & 0 & s_1 \end{pmatrix}. \tag{62}$$

Having the matrix $\mathcal{G}$ and S we can calculate the tunneling matrix

$$\mathcal{T}_{\alpha\mathbf{n},\beta\mathbf{m}} = \langle\phi_{\alpha\mathbf{n}}|\mathcal{H}|\phi_{\beta\mathbf{m}}\rangle = (\mathcal{G}^{\dagger}T\mathcal{G})_{\alpha\mathbf{n},\beta\mathbf{m}}, \tag{63}$$

where the entries of the matrix T are given as follows:

$$T_{\alpha\mathbf{n},\beta\mathbf{m}} = \langle\Psi_{\alpha\mathbf{n}}|\mathcal{H}|\Psi_{\beta\mathbf{m}}\rangle. \tag{64}$$

Since both the $|\Psi_{\alpha\mathbf{n}}\rangle$ and the $|\phi_{\alpha\mathbf{n}}\rangle$ states are localized at the lattice position $\mathbf{n}$, the matrices T and $\mathcal{T}$ both have the same nonzero entries as S. The tunneling matrix $\mathcal{T}$ has the same block form as S with $\mathcal{T}_{\mathrm{LL}} = \mathcal{T}_{\mathrm{RR}} = \epsilon_0\mathbb{1}$ and $\mathcal{T}_{\mathrm{LR}}$ having the same structure as S_{LR} with s_1 and s_2 replaced by t_1 and t_2, given as $t_1 = \mathcal{T}_{\mathbf{Ln},\mathbf{Rn}}$ and $t_2 = \mathcal{T}_{\mathbf{Ln},\mathbf{Rn}-\mathbf{e}_1} = \mathcal{T}_{\mathbf{Ln},\mathbf{Rn}+\mathbf{e}_2}$. The overlaps s_1 and s_2, together with the transition amplitudes t_1 and t_2, depend exponentially on the two parameters α and E_J/E_C. A detailed analysis is given below; here, we anticipate the approximate relations $t_1/t_2 > 1$ if $\alpha < 1$, $t_1/t_2 < 1$ if $\alpha > 1$, and $t_1/t_2 \approx 1$ if $\alpha = 1$, and $t_1/t_2 = 1$ if $C_1 = C_2 = 0$.

Now, we numerically determine the tunneling matrix elements t_1 and t_2 from Eqs. (63) and (64) and analyze their dependence on the external parameters. This dependence can then be used to control the qubit Hamiltonian. The external parameters fall into two categories, those that can be varied freely, like magnetic fields and bias voltages, and the device parameters, that are fixed for a specific device. Two main types of device parameters characterize the Hamiltonian: (i) the junction capacitance C_J that determines the charging energy $E_C = e^2/2C_J$ and (ii) the Josephson inductance L_J which determines the Josephson energy $E_J = (\Phi_0/2\pi)^2/L_J$. In addition, we have the ratio $\alpha = E_{J3}/E_J$.

The potential $\mathcal{U}(\boldsymbol{\varphi})$ can be modified in two ways. The external magnetic flux $\Phi_x = \Phi_0\varphi_x/2\pi$ is responsible for the symmetry of the double well within a unit cell and can give rise to a σ_z term in the single qubit Hamiltonian while α determines the height of the barrier between the wells in a cell and between two nearest neighbor unit cells. Thus α

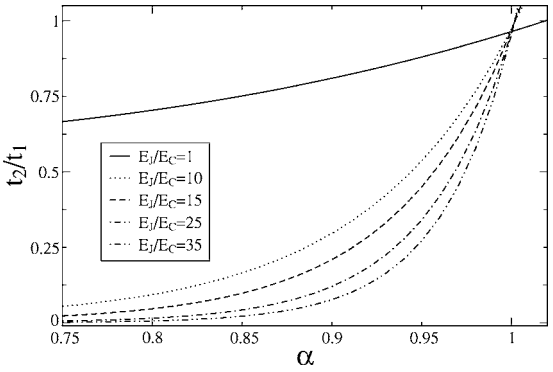

FIG. 5. The ratio t_2/t_1 between the tunneling matrix elements, plotted as a function of $\alpha \leqslant 1$ for several values of E_J/E_C.

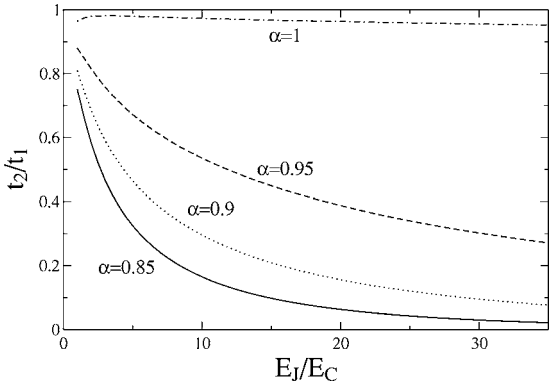

FIG. 6. The ratio t_2/t_1 between the tunneling matrix elements, plotted as a function of E_J/E_C for several values of $\alpha \leqslant 1$.

affects the values of the tunneling amplitudes between different sites in the lattice. Although α is a fixed device parameter for the setup shown in Fig. 1, a modified setup in which the middle junction is made flux tunable has been proposed;[1,3] a flux tunable junction is achieved by "shunting" the third junction with a further junction and using an external magnetic field to tune it.

In the tight-binding picture, the off-diagonal element Δ of the qubit Hamiltonian is a complex quantity that depends on the two tunneling amplitudes t_1 and t_2, whose relative strength can be set by α and the ratio E_J/E_C. The latter enters as a common factor into the frequencies of the Gaussian localized orbitals, determining the size of their overlaps and affecting only the energy gap $|\Delta|$. An increase of the value of α implies a decrease of the tunneling amplitudes t_1 and t_2, caused by an increase of the height of the barriers. Thus a careful choice of the two parameters is crucial in determining the behavior of the system. From Eq. (45), we find that if $t_2/t_1 \ll 1$ then Δ will be (almost) real. In order to obtain a sizable imaginary part of Δ, t_2/t_1 must be sufficiently large. In Fig. 5, we plot the ratio t_2/t_1 versus α, for several values of the E_J/E_C. Although all the curves approach the value $t_2/t_1 \approx 1$ for $\alpha \to 1$, as soon as $\alpha < 1$, a strong variation in t_2/t_1 is observed for large E_J/E_C. In Fig. 6, we plot t_2/t_1 versus E_J/E_C for different values of α. For $\alpha=1$, the curve is almost a constant. In Table I, we report a set of quantities calculated by varying both α and E_J/E_C, such as to keep the

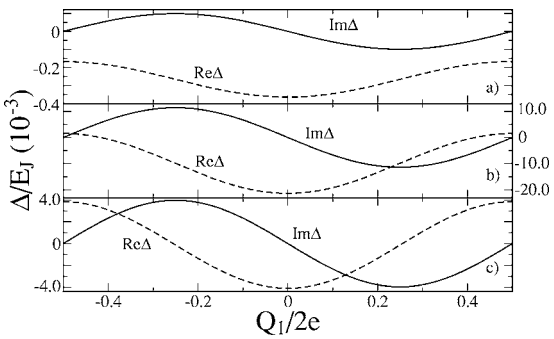

FIG. 7. Plot of the real and imaginary part of Δ as a function of $Q_1/2e=CV_1/2e$ for $CV_2/2e=0.5$ for (a) $\alpha=0.95$, $E_J/E_C=35$; (b) $\alpha=0.95$, $E_J/E_C=10$; and (c) $\alpha=1$, $E_J/E_C=15$.

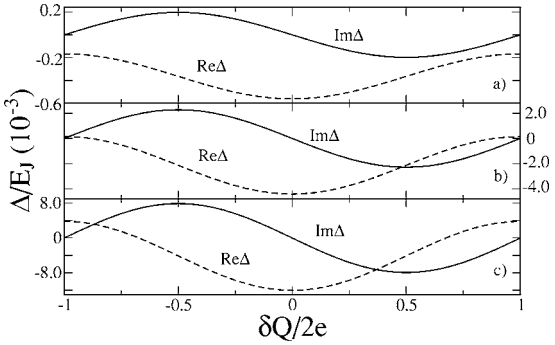

FIG. 8. Plot of the real and imaginary part of Δ as a function of $\delta Q/2e=C(V_1-V_2)/2e$ for $V_1+V_2=0$ choosing (a) $\alpha=0.95$, $E_J/E_C=35$, (b) $\alpha=0.95$, $E_J/E_C=10$ and (c) $\alpha=1$, $E_J/E_C=15$.

energy gap Δ_0 at zero applied voltage of the order of $\approx 0.1E_C$.

The parameters of an experimentally realized flux qubit (Delft qubit)[7] are $\alpha=0.8$ and $E_J/E_C=35$ and are given in the first row of Table I. In this case, the ratio t_2/t_1 is very small and the contribution of t_2 is negligible. This choice of parameters of the Delft qubit therefore does not allow the manifestation of a significant σ_y term in the single-qubit Hamiltonian, for any value of the bias voltage.

In Fig. 7, we plot the real and imaginary part of Δ as a function of the applied voltage V_1, expressed in the gate charge $Q_1=C_1V_1$, while keeping the other gate voltage fixed such that $Q_2/2e=C_2V_2/2e=0.5$. If the real part of Δ can be tuned from a finite value to zero while the imaginary part of Δ remains finite [as in Fig. 7(c)], then the pseudofield **B** can point along arbitrary angles in the equator plane of the Bloch sphere. The magnitude of the pseudofield can be controlled in principle by changing α, e.g., with a flux-tunable junction. In Fig. 8, we plot the real and imaginary part of Δ in the case where both voltages are varied simultaneously such that $V_1=-V_2$ as a function of $\delta Q/2e=C(V_1-V_2)/2e$. In Fig. 9 we plot the gap $|\Delta|$ as a function of $\delta Q/2e=C(V_1-V_2)/2e$ (solid line) and of $(Q_1+Q_2)/2e=C(V_1+V_2)/2e$ (dashed line) for this set of parameters.

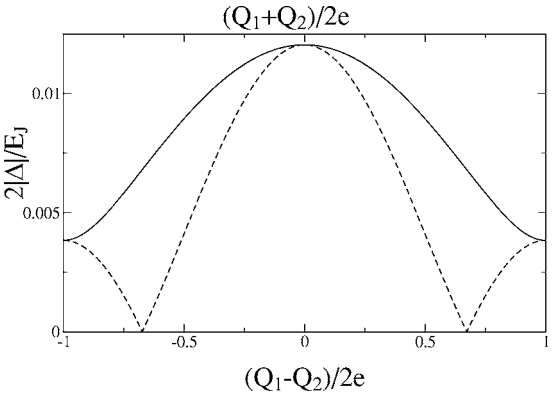

FIG. 9. Plot of the gap versus $\delta Q/2e=C(V_1-V_2)/2e$ (solid line) and $C(V_1+V_2)/2e$ (dashed line), for $\alpha=1$ and $E_J/E_C=15$. In this case both the amplitude of oscillation and the cross region of the curves are appreciable.

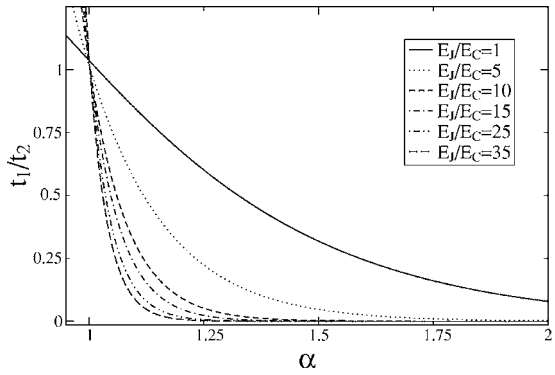

FIG. 10. The ratio t_1/t_2 between the tunneling matrix elements, plotted as a function of $\alpha \geqslant 1$ for several values of E_J/E_C.

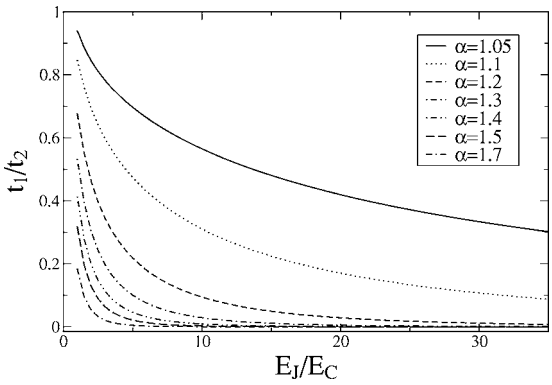

FIG. 11. The ratio t_1/t_2 between the tunneling matrix elements, plotted as a function of E_J/E_C for several values of $\alpha \geqslant 1$.

VII. FULL CONTROL FOR $\alpha > 1$

The flux qubit realized at Delft[7] operates with a ratio $\alpha = 0.8 < 1$ between the Josephson energies of its junctions. As shown in Table I, the ratio of tunneling matrix elements for this parameter choice is $t_2/t_1 = 0.0062$, thus the effect of the applied voltages is negligible. Two other regimes for α are interesting, namely $\alpha \approx 1$ and $\alpha > 1$.

In the former, t_1 and t_2 are approximately equal. In this case, $\boldsymbol{\varphi}$ can tunnel from a left minimum (L) to a right one (R) via both an intracell or an intercell tunneling process with almost equal probability. However, while intercell tunneling can be controlled via the applied voltages V_1 and V_2, allowing superposition with a nonzero relative phase of the qubit states, the intracell transition amplitude remains constant, once the parameters α and E_J/E_C are fixed, thus leading only to qubit flips. In Table I, for each value of $\alpha < 1$, the minimum of the gap is a finite quantity and can be calculated by the minimization of Eq. (46) with respect to $\mathbf{k}$. However, for $\alpha \geqslant 1$ there is a value of the external applied voltage for which the gap goes to zero (Fig. 9).

We are particularly interested in the regime $\alpha > 1$. In this case $t_1 < t_2$, i.e., the intracell tunneling between two minima is inhibited and, with a suitable choice of α, can be completely suppressed (Figs. 10 and 11). In this situation, the system can be described by a one-dimensional chain in which every even (odd) site is labeled as a "left" minimum L while the remaining sites are labeled "right" minima R, see Fig. 12. The tunneling matrix element between the sites is t_2 ($t_1 = 0$). Note that, due to the periodicity of the system, all L (R) sites have to be identified with each other, since they describe the same configuration.

From Eqs. (51) and (52), we immediately find that, for $t_1/t_2 \to 0$, we gain full control of the direction of the effective pseudofield $\mathbf{B}$ in the equatorial plane of the Bloch sphere, since

$$\Delta(k_+, k_-) = 4t_2 \cos(\pi k_+) e^{i\pi k_-}, \tag{65}$$

where $k_\pm = (C_1 V_1 \pm C_2 V_2)/2e$. The sum and difference of the gate charges therefore independently control the qubit energy gap and the angle θ of the pseudofield,

$$|\Delta| = 4|t_2 \cos(\pi k_+)|, \quad \theta = \pi k_-. \tag{66}$$

VIII. CHARGE DECOHERENCE

Voltage fluctuations from imperfect voltage sources or other fluctuating charges in the environment lead to charge fluctuations on the two islands in the circuit and thus to decoherence of the qubit. Moreover, we are considering here a situation where the sensitivity to external voltages has been deliberately enhanced and therefore it can be expected that charge fluctuations cannot be ignored. An estimate of the decoherence time for the same circuit has been developed in Ref. 10, where it is found to be 0.1 s.

In order to model bias voltage fluctuations, we include the two impedances Z_1 and Z_2 (Fig. 2) in our analysis. From circuit theory,[27] we can then obtain a Caldeira-Leggett model for the system coupled to its charge environment,

$$\mathcal{H} = \mathcal{H}_S + \mathcal{H}_B + \mathcal{H}_{SB}, \tag{67}$$

where $\mathcal{H}_S$ from Eq. (10) describes the dissipationless elements of the circuit, and

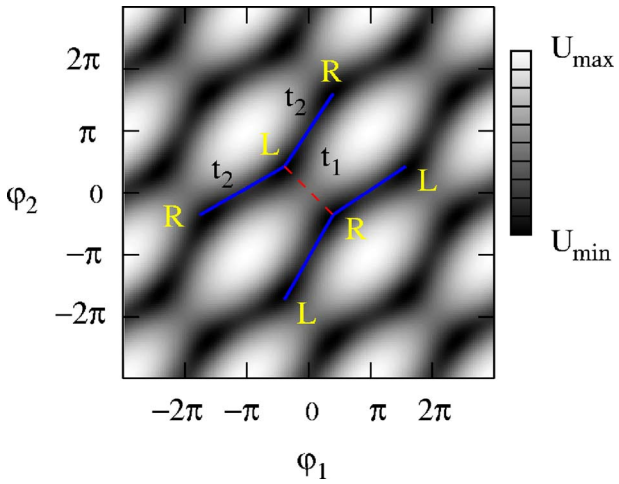

FIG. 12. (Color online) Density plot of the double well potential $U(\varphi_1, \varphi_2)$ for $\alpha = 1.4$, on a logarithmic scale. Two equivalent one-dimensional chains with nearest neighbor interaction are highlighted in the figure.

$$\mathcal{H}_B = \sum_{j=1,2} \sum_{\nu} \left(\frac{p_{j\nu}^2}{2m_{j\nu}} + \frac{1}{2} m_{j\nu} \omega_{j\nu}^2 x_{j\nu}^2 \right), \tag{68}$$

is the Hamiltonian of the degrees of freedom of two independent baths of harmonic oscillators that are used to model the two impedances, and finally

$$\mathcal{H}_{SB} = \sum_{j=1,2} \mathbf{m}_j \cdot \mathbf{Q} \sum_{\nu} c_{j\nu} x_{j\nu}, \tag{69}$$

describes the system-bath coupling, where $\mathbf{m}_1 = \mathcal{C}^{-1}(C_1, 0)^T$ and $\mathbf{m}_2 = \mathcal{C}^{-1}(0, C_2)^T$. The coupling constants $c_{j\nu}$ are related to Z_j via the spectral densities

$$J_j(\omega) = -\omega \operatorname{Re} Z_j(\omega) = \frac{\pi}{2} \sum_{\nu} \frac{c_{j\nu}^2}{m_{j\nu}\omega_{j\nu}} \delta(\omega - \omega_{j\nu}). \tag{70}$$

The decoherence rates in the Born-Markov approximation are given by (Ref. 27)

$$\frac{1}{T_1} = \frac{4}{\hbar^2} \sum_{j=1,2} |\mathbf{m}_j \cdot \langle 0|\mathbf{Q}|1\rangle|^2 \Delta \operatorname{Re} Z_j(\Delta) \coth \frac{\Delta}{2k_B T}, \tag{71}$$

$$\frac{1}{T_\phi} = \frac{1}{\hbar^2} \sum_{j=1,2} |\mathbf{m}_j \cdot (\langle 0|\mathbf{Q}|0\rangle - \langle 1|\mathbf{Q}|1\rangle)|^2 \operatorname{Re} Z_j(0) 2k_B T. \tag{72}$$

Now we compute the matrix elements of the charge operator $\mathbf{Q} = -2ie\boldsymbol{\nabla}$ in the $|0\rangle$, $|1\rangle$ basis. Following the derivation of the Hamiltonian in Sec. V B, we start from:

$$\langle u_{\alpha\mathbf{k}}|\mathbf{Q}|u_{\beta\mathbf{k}}\rangle = -2e\mathbf{k}\delta_{\alpha\beta} - 2ie\langle \psi_{\alpha\mathbf{k}}|\boldsymbol{\nabla}|\psi_{\beta\mathbf{k}}\rangle. \tag{73}$$

The matrix elements of $\mathbf{Q}$ between the Bloch states

$$\langle \psi_{\alpha\mathbf{k}}|\mathbf{Q}|\psi_{\beta\mathbf{k}}\rangle = \sum_{\mathbf{n},\mathbf{m}\in\mathbb{Z}^2} e^{2\pi i\mathbf{k}\cdot(\mathbf{n}-\mathbf{m})} \mathbf{Q}_{\alpha\mathbf{m},\beta\mathbf{n}}, \tag{74}$$

are given in terms of the matrix elements of $\boldsymbol{\nabla}$ between the Wannier functions

$$\mathbf{Q}_{\alpha\mathbf{n},\beta\mathbf{m}} = -2ei\langle \phi_{\alpha\mathbf{n}}| \boldsymbol{\nabla} |\phi_{\beta\mathbf{m}}\rangle = -2ei(\mathcal{G}^T \mathbf{P} \mathcal{G})_{\alpha\mathbf{n},\beta\mathbf{m}}, \tag{75}$$

and, in turn, through the $\mathcal{G}$ matrix, they are expressed in terms of the Gaussian states,

$$\mathbf{P}_{\alpha\mathbf{n},\beta\mathbf{m}} = \langle \Psi_{\alpha\mathbf{n}}| \boldsymbol{\nabla} |\Psi_{\beta\mathbf{m}}\rangle = \frac{1}{2} \mathcal{M} \Delta\boldsymbol{\varphi}_{\alpha\mathbf{n},\beta\mathbf{m}} S_{\alpha\mathbf{n},\beta\mathbf{m}}, \tag{76}$$

where the matrix $\mathcal{M}$ is defined in Eq. (28), $\Delta\boldsymbol{\varphi}_{\alpha\mathbf{n},\beta\mathbf{m}} = \boldsymbol{\varphi}_\beta - \boldsymbol{\varphi}_\alpha + 2\pi(\mathbf{m}-\mathbf{n})$, and the S matrix is defined in Eq. (58).

We only keep the leading matrix elements s_1 and s_2 in the overlap matrix S when calculating the $\mathcal{G}$ and $\mathbf{P}$ matrices (see Sec. VI). Since the largest contributions of $\mathbf{P}$ are proportional to s_1 and s_2, we can use $\mathcal{G} \approx \mathbb{1}$, and thus $\mathbf{Q}_{\alpha\mathbf{n},\beta\mathbf{m}} \simeq \mathbf{P}_{\alpha\mathbf{n},\beta\mathbf{m}} \propto \mathbf{S}_{\alpha\mathbf{n},\beta\mathbf{m}}$. We consider the diagonal term and the off-diagonal term separately and obtain,

$$\langle u_{\alpha\mathbf{k}}|\mathbf{Q}|u_{\alpha\mathbf{k}}\rangle = -\mathbf{Q}_g, \tag{77}$$

$$\langle u_{\mathrm{L}\mathbf{k}}|\mathbf{Q}|u_{\mathrm{R}\mathbf{k}}\rangle = -ei\mathcal{M}[s_1\Delta\boldsymbol{\varphi} + s_2(\Delta\boldsymbol{\varphi} - 2\pi\mathbf{e}_1)e^{2\pi i k_1} + s_2(\Delta\boldsymbol{\varphi} + 2\pi\mathbf{e}_2)e^{-2\pi i k_2}], \tag{78}$$

where s_1, s_2, $\Delta\boldsymbol{\varphi} = \boldsymbol{\varphi}_\mathrm{R} - \boldsymbol{\varphi}_\mathrm{L}$, and the matrix $\mathcal{M}$ depend on $\alpha = E_{J3}/E_J$ and E_J/E_C. In the qubit basis we find,

$$\langle 0|\mathbf{Q}|0\rangle - \langle 1|\mathbf{Q}|1\rangle = -e\mathcal{M}[s_1 \sin(\theta)\Delta\boldsymbol{\varphi} + s_2 \sin(\theta + 2\pi k_1) \times (\Delta\boldsymbol{\varphi} - 2\pi\mathbf{e}_1) + s_2 \sin(\theta - 2\pi k_2) \times (\Delta\boldsymbol{\varphi} + 2\pi\mathbf{e}_2)], \tag{79}$$

$$\langle 0|\mathbf{Q}|1\rangle = ie\mathcal{M}[s_1 \cos(\theta)\Delta\boldsymbol{\varphi} + s_2 \cos(\theta + 2\pi k_1)(\Delta\boldsymbol{\varphi} - 2\pi\mathbf{e}_1) + s_2 \cos(\theta - 2\pi k_2)(\Delta\boldsymbol{\varphi} + 2\pi\mathbf{e}_2)], \tag{80}$$

where $\tan\theta = \operatorname{Im}\Delta/\operatorname{Re}\Delta$ is a function of $k_{1,2} = C_{1,2}V_{1,2}/2e$. Using Eqs. (71), (72), (79), and (80) we can express the decoherence rates in a more explicit way,

$$\frac{1}{T_1} = 2\pi \frac{E_J}{\hbar} \frac{\operatorname{Re} Z}{R_Q} \left(\frac{C}{C_J} \right)^2 s_2^2 \mathcal{F}_1(V_1, V_2), \tag{81}$$

$$\frac{1}{T_\phi} = 2\pi \frac{2k_B T}{\hbar} \frac{\operatorname{Re} Z}{R_Q} \left(\frac{C}{C_J} \right)^2 s_2^2 \mathcal{F}_\phi(V_1, V_2), \tag{82}$$

where s_2, $\mathcal{F}_1$, and $\mathcal{F}_\phi$ are given in Appendix C. $\mathcal{F}_1$ and $\mathcal{F}_\phi$ are periodic functions of the applied voltages V_1 and V_2 that depend on the parameters α, E_J/E_C, and on s_1/s_2. They can be estimated to be at most of order one, depending on the choice of parameters and the applied voltages. In Eqs. (81) and (82) we chose $Z \approx Z_1 \approx Z_2$, and $R_Q = h/e^2$ is the quantum of resistance.

In the regime $\alpha > 1$ we have $s_2 \gg s_1$. For $\alpha = 1.4$, $E_J/E_C = 15$, and $C/C_J = 0.02$ we find that $s_2 = 8 \times 10^{-4}$. An estimate for $T \approx 100$ mK, $\mathrm{Re}Z \approx 1$ kΩ, and $E_J = 250$ GHz produces decoherence times in the millisecond range,

$$\frac{1}{T_1} \simeq \frac{\mathcal{F}_1(V_1, V_2)}{\mathcal{F}_{1,\max}} \frac{1}{6\ \mathrm{ms}}, \tag{83}$$

$$\frac{1}{T_\phi} \simeq \frac{\mathcal{F}_\phi(V_1, V_2)}{\mathcal{F}_{\phi,\max}} \frac{1}{12\ \mathrm{ms}}. \tag{84}$$

For some particular values of V_1 and V_2 the functions $\mathcal{F}_1$ or $\mathcal{F}_\phi$ vanish, implying that $1/T_1 \to 0$ or $1/T_\phi \to 0$. In particular, $\mathcal{F}_1 = 0$ for $(C_1V_1, C_2V_2)/2e = \pm(1/2, 0)$, $\pm(0, 1/2)$, $\pm(1/4, 1/4)$, $\pm(1/8, -1/8)$, $\pm(3/8, -3/8)$ in the FBZ, and $\mathcal{F}_\phi = 0$ for $(C_1V_1, C_2V_2)/2e = (n/2, m/2)$, $\pm(1/4, -1/4) + (n, m)$, with $n, m \in \mathbb{Z}$. The two functions have a common set of zeros, namely $\pm(n/2, 0)$, $\pm(0, m/2)$, with $n, m \in \mathbb{Z}$. In these cases, both $1/T_1$, $1/T_\phi \to 0$.

For the regime $\alpha < 1$ we have that $s_1 \gg s_2$ and we can neglect terms containing s_2. Choosing $\alpha = 0.8$ and $E_J/E_C = 35$ we find $s_1 = 1.3 \times 10^{-5}$. It follows that the decoherence rates are strongly suppressed and an estimate shows that they are below 1 Hz. This means that in this case the main process that causes decoherence is not due to the charge degrees of freedom. In fact for the Delft qubit[7] that operates in this

regime, the dephasing and the relaxation times caused by other mechanisms are much smaller, $T_\phi = 20$ ns and $T_1 = 900$ ns.

The physical reason for the small decoherence and relaxation rates found here is that, despite the voltage bias, we are still dealing with a flux qubit whose states are indistinguishable from their charge distribution, as seen from Eq. (77).

IX. RESULTS AND CONCLUSIONS

By means of circuit theory and a tight-binding approximation, we have analyzed a voltage-controlled SC flux qubit circuit that allows full control of the single-qubit Hamiltonian Eq. (50), with σ_x, σ_y, and σ_z terms, in order to allow arbitrary single qubit operations.

One of the main results of this work is the computation of the tunneling matrix elements appearing in the single qubit Hamiltonian as a function of the device parameters α and E_J/E_C. This allowed us to explore new possible working regimes of the system, looking for a range of parameters for which a full control on qubit rotations is feasible. Substantially, the qubit can work in two different regimes, $\alpha < 1$ and $\alpha > 1$, showing different features. In particular, for $\alpha > 1$, the pseudomagnetic field **B** that couples to the qubit in the Hamiltonian has a nonzero y component. This allows full control of qubit rotations on the Bloch sphere through the applied voltages V_1 and V_2. In fact, in the Hamiltonian, Eq. (50), the off-diagonal term Δ, given in Eq. (45), contains the voltages $V_{1,2}$ and the sensitivity to $V_{1,2}$ is determined by the tunneling parameters t_1 and t_2 in Eqs. (41) and (43).

For $\alpha \leqslant 1$, we find $t_1 \gtrsim t_2$. The effect of t_2, and thus of the applied voltages, for the value of parameters of the Delft qubit,[7] is negligible as shown in Table I, but can be greatly enhanced for a suitable choice of α and E_J/E_C (see Figs. 5 and 6), thus allowing good control in the real and imaginary parts of Δ, as shown in Eqs. (51) and (52) and in Figs. 7 and 8.

In the case $\alpha > 1$, the roles of t_1 and t_2 are interchanged, as shown in Figs. 10 and 11, and a regime in which a full control of the single-qubit Hamiltonian becomes possible. For a suitable choice of α and E_J/E_C, the tunneling parameter t_1 become vanishingly small, giving rise to a simple dependence of Δ on the voltages, as found in Eqs. (65) and (66).

Our analysis is based on the two-level approximation, i.e., we assume that we can neglect all high levels besides the two lowest ones. This approximation is justified if the energy gap E_{12} between the two lowest levels and any higher level is sufficiently large, in particular, larger than the qubit gap $E_{01} = |\Delta|$. The gap E_{12} can be roughly estimated as the plasma frequency, i.e., the smallest of the frequencies of the (anisotropic) harmonic oscillator arising from the linearization of the equation of motion around the minimum configurations of the potential. This frequency is given by (also see Appendix B) $\omega_{LC} = 1/\sqrt{C_J L_J} = \sqrt{8E_J E_C}/\hbar$. In Table I, we report the ratio of E_{12} and the qubit gap $|\Delta_0|$ at zero applied voltage. For all parameter values studied, E_{12} exceeds $2|\Delta_0|$ by more than a factor of 20, in many relevant cases even by two orders of magnitude, thus justifying the two-level approximation.

Finally, we have studied the decoherence due to charge fluctuations of the voltage sources. Our result for the T_1^{-1} and T_ϕ^{-1} rates is given in Eqs. (81) and (82), an estimate of which yields a coherence time longer than ≈ 1 ms, leading to the conclusion that charge fluctuations are not the main source of decoherence, even in the regime in which the sensitivity to external voltages is enhanced. The coherence of the system is well preserved, since the qubit is still essentially a SC flux qubit, i.e., the $|0\rangle$ and $|1\rangle$ states have nearly identical charge configurations.

In conclusion, based on our analysis we find that full control of single-qubit operations in a SC flux qubit should be feasible, provided that the right choice of the device parameters is made.

ACKNOWLEDGMENTS

We would like to thank David DiVincenzo for very useful discussions. We acknowledge financial support from the Swiss National Science Foundation.

APPENDIX A: MATRICES $\mathcal{C}$, $\mathbf{C}_V$, $\mathbf{M}_0$, AND $\mathbf{N}$

The definitions of the derived matrices $\mathcal{C}$, $\mathbf{C}_V$, $\mathbf{M}_0$, and $\mathbf{N}$ that enter the Hamiltonian are given in Refs. 26 and 27 for the general case. Here we apply the theory and derive the matrices for the particular case of the circuit of Fig. 2. The derived capacitance matrices are

$$\mathcal{C} \equiv \mathbf{C}_J + \begin{pmatrix} \mathbf{C} & 0 \\ 0 & 0 \end{pmatrix}, \tag{A1}$$

$$\mathbf{C}_V \equiv (\mathbf{C}, 0)^T. \tag{A2}$$

The inductance matrices that enter the potential are

$$\mathbf{M}_0 = \frac{1}{K}\mathbf{F}_{JK}\mathbf{F}_{JK}^T, \tag{A3}$$

$$\mathbf{N} = -\frac{1}{K}\mathbf{F}_{JK}, \tag{A4}$$

and $\mathbf{M}_0^T = \mathbf{M}_0$. For the circuit studied here, we obtain

$$\mathbf{M}_0 = \frac{1}{K}\begin{pmatrix} 1 & -1 & -1 \\ -1 & 1 & 1 \\ -1 & 1 & 1 \end{pmatrix}, \quad \mathbf{N} = \frac{1}{K}\begin{pmatrix} 1 \\ -1 \\ -1 \end{pmatrix}. \tag{A5}$$

APPENDIX B: PROJECTED MATRICES

The three-dimensional problem is mapped into a two-dimensional one in Sec. III with the matrix

$$\mathcal{P} = \begin{pmatrix} 1 & 0 \\ 0 & 1 \\ 1 & -1 \end{pmatrix}, \tag{B1}$$

via the relation $(\varphi_1, \varphi_2, \varphi_3)^T = \mathcal{P}(\varphi_1, \varphi_2)^T$. In the case of symmetric double well potential, the inductance linearized matrix $\mathbf{L}_{\mathrm{lin;L,R}}^{-1}$ is given by

$$\mathbf{L}^{-1}_{\mathrm{lin;L,R}} = \mathbf{M}_0 + \mathbf{L}_J^{-1} \cos \boldsymbol{\varphi}_{\mathrm{L,R}}. \tag{B2}$$

Because of the symmetry of the potential, we drop the subscripts R and L. Applying the matrix $\mathcal{P}$ we obtain $\mathbf{L}^{-1}_{\mathrm{lin},P} = \mathcal{P}^T \mathbf{L}^{-1}_{\mathrm{lin}} \mathcal{P}$,

$$\mathbf{L}^{-1}_{\mathrm{lin},P} = \frac{1}{L_J} \begin{pmatrix} \alpha & \frac{1}{2\alpha} - \alpha \\ \frac{1}{2\alpha} - \alpha & \alpha \end{pmatrix}. \tag{B3}$$

In order to simplify the calculation we assume the two capacitance C_1 and C_2 to be equal, $C_1 = C_2 \equiv C$ and define $\gamma = C/C_J$. The projected capacitance matrix $\mathcal{C}_P = \mathcal{P}^T \mathcal{C} \mathcal{P}$ is then found to be

$$\mathcal{C}_P = C_J \begin{pmatrix} 1+\gamma+\alpha & -\alpha \\ -\alpha & 1+\gamma+\alpha \end{pmatrix}. \tag{B4}$$

In this case, the orthogonal matrices that diagonalize the capacitance matrix $\mathcal{C}_P$ the linearized inductance matrix $\mathbf{L}^{-1}_{\mathrm{lin},P}$ are identical, $\mathcal{C}_P = \mathbf{O}^T \mathcal{C}_d \mathbf{O}$ and $\mathbf{L}^{-1}_{\mathrm{lin},P} = \mathbf{O}^T \Lambda \mathbf{O}$. The frequency matrix $\Omega = \mathrm{diag}(\omega_\perp, \omega_\parallel)$ is given by

$$\boldsymbol{\Omega}^2 = \omega_{LC}^2 \begin{pmatrix} \frac{1}{4\alpha^2(1+\gamma)^2} & 0 \\ 0 & \frac{1-4\alpha^2}{4\alpha^2(1+2\alpha+\gamma)^2} \end{pmatrix}, \tag{B5}$$

where $\omega_{LC}^2 = 1/L_J C_J$. The matrix $\mathcal{M}$ is then diagonalized by the same orthogonal matrix $\mathbf{O}$ and, in the basis where it is diagonal, can be written

$$\mathcal{M} = \sqrt{\frac{E_J}{8E_C}} \begin{pmatrix} \sqrt{\frac{1+\gamma}{2\alpha}} & 0 \\ 0 & \sqrt{\frac{(4\alpha^2-1)(1+2\alpha+\gamma)}{2\alpha}} \end{pmatrix}. \tag{B6}$$

APPENDIX C: THE FUNCTIONS $\mathcal{F}_1$ AND $\mathcal{F}_\phi$

We give here an explicit formula for the intracell and intercell overlaps s_1 and s_2 as functions of α, E_J/E_C and C/C_J,

$$s_1 = \exp\left\{ -\frac{E_J}{4\sqrt{2\alpha} E_C} \times \arccos^2\left(\frac{1}{2\alpha}\right) \sqrt{(4\alpha^2-1)(1+2\alpha+C/C_J)} \right\}, \tag{C1}$$

$$s_2 = \exp\left\{ -\frac{E_J}{16E_C} \left[\pi^2 \sqrt{\frac{1+C/C_J}{2\alpha}} + \left(\pi - 2 \times \arccos\left(\frac{1}{2\alpha}\right) \right)^2 \sqrt{\frac{(4\alpha^2-1)(1+2\alpha+C/C_J)}{2\alpha}} \right] \right\}. \tag{C2}$$

Through these quantities we can express $\mathcal{F}_1$ and $\mathcal{F}_\phi$ as functions of k_1 and k_2, with $k_i = C_i V_i / 2e$,

$$\mathcal{F}_1(k_1,k_2) = \frac{|\Delta(k_1,k_2)|}{E_J} \coth\left(\frac{|\Delta(k_1,k_2)|}{2k_B T} \right) \tilde{\mathcal{F}}_\phi(k_1,k_2), \tag{C3}$$

$$\mathcal{F}_\phi(k_1,k_2) = \frac{4}{\det^2(\mathcal{C})} \sum_{i=1,2} \Big[\pi (\mathcal{C}_{1i}\mathcal{M}_{22} \sin(2\pi k_2 - \theta) - \mathcal{C}_{2i}\mathcal{M}_{11} \sin(2\pi k_1 + \theta)) + (\mathcal{C}_{2i}\mathcal{M}_{11} + \mathcal{C}_{1i}\mathcal{M}_{22}) \arccos\left(\frac{1}{2\alpha}\right) \times \left(\frac{s_1}{s_2} \sin(\theta) + \sin(2\pi k_1 + \theta) - \sin(2k_2 - \theta) \right) \Big]^2, \tag{C4}$$

where $\tilde{\mathcal{F}}_\phi$ is given by $\mathcal{F}_\phi$, once the sin are replaced by cos. $\mathcal{C}_{ij}$ and $\mathcal{M}_{ij}$ are the entries of the matrices $\mathcal{C}$ and $\mathcal{M}$ defined in Appendix B. The gap $|\Delta|$ and the relative phase between the states $|0\rangle$ and $|1\rangle$ are given by

$$|\Delta(k_1,k_2)| = 2\sqrt{(t_1 + 2t_2 \cos[\pi(k_1-k_2)] \cos[\pi(k_1+k_2)])^2 + 4t_2^2 \cos[\pi(k_1+k_2)] \sin[\pi(k_1-k_2)]}, \tag{C5}$$

$$\tan\theta = \frac{2t_2 \cos[\pi(k_1+k_2)] \sin[\pi(k_1-k_2)]}{t_1 + 2t_2 \cos[\pi(k_1-k_2)] \cos[\pi(k_1+k_2)]}. \tag{C6}$$

[1] Y. Makhlin, G. Schön, and A. Shnirman, Rev. Mod. Phys. **73**, 357 (2001).

[2] M. H. Devoret, A. Wallraff, and J. M. Martinis, cond-mat/0411174 (unpublished).

[3] T. P. Orlando, J. E. Mooij, L. Tian, C. H. van der Wal, L. Levitov, S. Lloyd, and J. J. Mazo, Phys. Rev. B **60**, 15398 (1999).

[4] J. E. Mooij, T. P. Orlando, L. Levitov, L. Tian, C. H. van der Wal, and S. Lloyd, Science **285**, 1036 (1999).

[5] J. R. Friedman, V. Patel, W. Chen, S. K. Tolpygo, and J. E. Lukens, Nature (London) **406**, 43 (2000).

[6] C. H. van der Wal, A. C. J. ter Haar, F. K. Wilhelm, R. N. Schouten, C. J. P. M. Harmans, T. P. Orlando, S. Lloyd, and J. E. Mooij, Science **290**, 773 (2000).
[7] I. Chiroescu, Y. Nakamura, C. J. P. M. Harmans, and J. E. Mooij, Science **299**, 1869 (2003).
[8] P. Bertet, I. Chiorescu, G. Burkard, K. Semba, C. J. P. M. Harmans, D. P. DiVincenzo, and J. E. Mooij, Phys. Rev. Lett. **95**, 257002 (2005).
[9] F. Yoshihara, K. Harrabi, A. O. Niskanen, Y. Nakamura, and J. S. Tsai, Phys. Rev. Lett. **97**, 167001 (2006).
[10] L. Tian, L. S. Levitov, C. H. van der Wal, J. E. Mooij, T. P. Orlando, S. Lloyd, C. J. P. M. Harmans, and J. J. Mazo, in *Quantum Mesoscopic Phenomena and Mesoscopic Devices in Microelectronics*, edited by I. O. Kulik and R. Ellialtioglu (Kluwer, Dordrecht, 2000), pp. 429–438.
[11] L. Tian, S. Lloyd, and T. P. Orlando, Phys. Rev. B **65**, 144516 (2002).
[12] C. H. van der Wal, F. K. Wilhelm, C. J. P. M. Harmans, and J. E. Mooij, Eur. Phys. J. B **31**, 111 (2003).
[13] D. V. Averin, Solid State Commun. **105**, 659 (1998).
[14] Y. Makhlin, G. Schön, and A. Shnirman, Nature (London) **398**, 305 (1999).
[15] Y. Nakamura, Yu, A. Pashkin, and J. S. Tsai, Nature (London) **398**, 786 (1999).
[16] Y. A. Pashkin, T. Yamamoto, O. Astafiev, Y. Nakamura, D. V. Averin, and J. S. Tsai, Nature (London) **421**, 823 (2003).
[17] T. Yamamoto, Y. A. Pashkin, O. Astafiev, Y. Nakamura, and J. S. Tsai, Nature (London) **425**, 941 (2003).
[18] D. Vion, A. Aassime, A. Cottet, P. Joyez, H. Pothier, C. Urbina, D. Esteve, and M. H. Devoret, Science **296**, 886 (2002).
[19] J. M. Martinis, S. Nam, J. Aumentado, and C. Urbina, Phys. Rev. Lett. **89**, 117901 (2002).
[20] M. H. S. Amin, Phys. Rev. B **71**, 024504 (2005).
[21] M. H. S. Amin, Phys. Rev. B **71**, 140505(R) (2005).
[22] G. Falci, R. Fazio, G. M. Palma, J. Siewert, and V. Vedral, Nature (London) **407**, 355 (2000).
[23] D. Aharonov, W. van Dam, J. Kempe, Z. Landau, S. Lloyd, and O. Regev, quant-ph/0405098 (unpublished).
[24] R. Oliveira and B. M. Terhal, quant-ph/0504050 (unpublished).
[25] S. Bravyi, B. M. Terhal, and D. P. DiVincenzo (unpublished).
[26] G. Burkard, R. H. Koch, and D. P. DiVincenzo, Phys. Rev. B **69**, 064503 (2004).
[27] G. Burkard, Phys. Rev. B **71**, 144511 (2005).
[28] G. Burkard, D. P. DiVincenzo, P. Bertet, I. Chiorescu, and J. E. Mooij, Phys. Rev. B **71**, 134504 (2005).
[29] D. P. DiVincenzo, F. Brito, and R. H. Koch, Phys. Rev. B **74**, 014514 (2006).
[30] D. V. Averin, A. B. Zorin, and K. K. Likharev, Sov. Phys. JETP **61**, 407 (1985).
[31] K. K. Likharev and A. B. Zorin, J. Low Temp. Phys. **59**, 347 (1985).
[32] M. Iansiti, M. Tinkham, A. T. Johnson, W. F. Smith, and C. J. Lobb, Phys. Rev. B **39**, 6465 (1989).